



Activating Fe activity and improving Ni activity via C_3N_4 substrate in alkaline oxygen evolution catalyzed by Ni-Fe phosphide

Hongyan Zhang^a, Tao Yang^{a,b,*}, Hao Zhou^a, Yikai Wang^a, Xuehan Yang^a, Wenjie Liang^a, Dan Wu^a, Pan Yuan^a, Tingting Yu^a, Maoshuai He^c, Wenxian Wei^d

^a School of Environmental and Chemical Engineering, Jiangsu Key Laboratory of Marine Bioresources and Environment, Jiangsu Key Laboratory of Marine Biotechnology, Jiangsu Ocean University, Lianyungang 222005, China

^b Co-Innovation Center of Jiangsu Marine Bio-industry Technology, Jiangsu Ocean University, Lianyungang 222005, China

^c Key Laboratory of Eco-Chemical Engineering, Ministry of Education, College of Chemistry and Molecular Engineering, Qingdao University of Science and Technology, Qingdao 266042, China

^d Testing Center, Yangzhou University, Yangzhou 225009, China

ARTICLE INFO

Keywords:

Oxygen evolution
Water splitting
Hydrogen production
Non-precious metal catalysts
Ni-based catalysts

ABSTRACT

Ni phosphides have recently attracted considerable attention as promising catalysts for the oxygen evolution reaction (OER) and are generally promoted by Fe incorporation. However, the catalytic performance of nickel phosphide still does not meet the desired expectations. Additionally, the catalytic activity of iron (Fe) is insignificant and can be disregarded. In this study, we used C_3N_4 as a carbon substrate to modulate the 3d electron configurations and adsorption properties of Ni and Fe. Density functional theory (DFT) analysis reveals that the catalytic performance of Ni sites can be enhanced by utilizing the C_3N_4 substrate. Surprisingly, the Fe sites can also be activated to catalyze OER through a direct O_2 mechanism and the catalytic activity of Fe is found to surpass that of Ni. As a result, the FeNi- C_3N_4 -P catalyst demonstrated remarkable catalytic performance for OER. It exhibited a Tafel slope of 40.4 mV dec^{-1} , an overpotential of 235 mV at 100 mA cm^{-2} , and exhibited exceptional stability. This study highlights the activation of Fe and the enhancement of Ni by utilizing nitrogen-containing carbon substrates. This strategy offers promising prospects for the development of efficient Ni/Fe-based OER catalysts.

1. Introduction

Hydrogen has become a very promising energy carrier, providing a viable solution to the increasingly serious problems of environmental pollution and energy crisis [1,2]. Among the various hydrogen production technologies available, electrochemical water splitting has been significant recognized as a clean and environmentally friendly approach. This method utilizes electrical energy to convert water into hydrogen, offering a sustainable and mild condition process for the production of green hydrogen [3,4]. The oxygen evolution reaction (OER), which involves the formation, adsorption/desorption and transformation behavior of complex intermediates in the multi-proton coupled electron transfer (PCET) process, is the decisive bottleneck to improve water splitting technology [5–7]. Although precious metal-based catalysts such as IrO_2 and RuO_2 are highly efficient, they

still require a significant overpotential to provide the required OER current density. In addition, their high cost and scarcity have severely hindered their widespread use in commercial applications [8]. Therefore, scientists have extensively studied the earth abundant first-row (3d) transition metal-based materials in pursuit of efficient, economical, long-life OER electrocatalysts [9].

Among all kinds of transition metal-based OER catalysts, nickel-based catalysts, especially nickel phosphide, have great application prospects because of their highly adjustable electronic configurations [10–12]. Phosphorus (P) has a unique electron-orbital configuration with 3p unpaired electrons and 3d vacant orbitals. This configuration not only increases the local charge density but also has a strong electron accommodating capacity [13]. It has been revealed that OER activity is mainly affected by the adsorption/desorption behavior of OER intermediates (*OH, *O and *OOH) on the catalyst surface, which is

* Corresponding author at: School of Environmental and Chemical Engineering, Jiangsu Key Laboratory of Marine Bioresources and Environment, Jiangsu Key Laboratory of Marine Biotechnology, Jiangsu Ocean University, Lianyungang 222005, China.

E-mail addresses: 2007000037@jou.edu.cn, yangtao_hit@163.com (T. Yang).

<https://doi.org/10.1016/j.apcatb.2023.123391>

Received 31 August 2023; Received in revised form 3 October 2023; Accepted 9 October 2023

Available online 11 October 2023

0926-3373/© 2023 Elsevier B.V. All rights reserved.

mainly determined by the electron configuration of the catalytic site [14]. The valence electron configuration of Ni^{2+} is $3d^8$ ($t_{2g}^6 e_g^2$), and the main interaction between the fully occupied t_{2g} d -orbitals of Ni^{2+} and the bridging O is strong electron-electron repulsion, which results in too weak adsorption of oxygen-containing intermediates at the Ni site [15]. To solve this problem, an effective solution is to design nickel-based catalysts by incorporating highly oxygenophilic elements such as Fe [16–18]. Unlike Ni's fully occupied π -symmetric d -orbitals (t_{2g}^6), Fe has unpaired electrons in the same π -symmetric d -orbitals (t_{2g}^3), resulting in a weak repulsion with O. The strong and weak interaction of Ni/O and Fe/O will result in electron donation from Ni to Fe through the Ni-O-Fe bond. This electron redistribution enhances the adsorption of key intermediates at the Ni site [19]. Consequently, Fe can accelerate the decomposition of $^*\text{OOH}$ into O_2 at the adjacent Ni sites [20]. In addition to modulating the $3d$ electronic configuration of Ni, it has been reported that Fe can also participate in the OER process. $^*\text{OOH}$ formation is generally considered to be the rate-determining step (RDS) of OER [21]. A Fe-Ni bimetal catalyst can promote the formation of $^*\text{OOH}$ by adsorbing $^*\text{O}$ to the Ni sites and bonding $^*\text{OH}$ to the adjacent Fe sites [22]. The hetero-interface of $\text{Ni}_2\text{P}(\text{O})/\text{Fe}_2\text{P}(\text{O})$ based on the similar principle significantly improved catalytic performance [13].

However, the catalytic performance of Ni-Fe based catalysts still has not reached the expectation of wide application. One of the reasons is that modulation of the electron configuration of Ni by Fe is limited and inadequate. Even in a ternary system such as FeCoW, the optimized adsorption/desorption energies is limited by the metals involved and cannot be adjusted at a larger scale, nor can the electron/adsorption configurations be adjusted with greater diversity [23]. Another reason is that Fe, as an important metal element in Fe-Ni phosphides, has not been fully investigated and utilized for its catalytic activity [24]. Studies have shown that in Ni-Fe layered double hydroxides (LDHs), the turnover frequencies (TOFs) of Fe sites are 20–200 times higher than that of the Ni site, and when the Fe content exceeded 4.7 %, the Fe site dominated the catalysis [25]. Therefore, with appropriate strategies, it is very possible that Fe in Fe-Ni phosphides can be activated and raised to higher levels, even exceeding the activity of Ni sites.

In recent years, there has been a growing interest in using carbonaceous substrates to precisely modulate the electronic structure of transition metal active sites. This approach presents an intriguing and challenging way to explore efficient catalysts [22]. The carbonaceous substrate provides a multi-dimensional porous network with abundant mass diffusion pathways and excellent electrical conductivity. More catalytic sites with higher activity can also be generated at the metal/carbon hetero-interface [26,27]. In addition, charge transfer at the interface between the carbon substrate and the metal atoms can optimize the electron configuration of the active site, which in turn changes the adsorption/desorption behavior of the reaction intermediates [28, 29].

Graphitic carbon nitride (g- C_3N_4) is a two-dimensional carbonaceous material with a structure similar to graphene. It consists of tertiary amine-linked periodic heptazine unit [30]. The presence of nitrogen in g- C_3N_4 has two advantages. Firstly, nitrogen atoms can form coordination bonds with metal atoms in the form of M-Nx, changing the electron configuration of the metal atom by sharing a lone pair of electrons [30–32]. Therefore, g- C_3N_4 supported metal-based materials have been widely used as electrocatalysts for oxygen reduction and evolution [31]. Secondly, since the nitrogen in g- C_3N_4 has more delocalized electrons, the adsorption of the intermediate at the active metal site is enhanced [32]. This enhanced adsorption can improve the catalytic activity and stability of the catalyst. Overall, using g- C_3N_4 as substrates can achieve precise regulation of transition metal electronic structures in more forms and in a wider range.

In this study, we have successfully constructed an interfacial hetero-structure of FeNi phosphide/ C_3N_4 (FeNi- C_3N_4 -P) to regulate the valence electronic configurations of Ni and Fe, aiming to develop an efficient OER catalyst. The highly electronegative N atoms in C_3N_4 are expected

to attract electrons from metal atoms, thus strengthening the adsorption of OER intermediates at Ni sites. On the other hand, the N atoms in C_3N_4 are presumed to share their lone-paired electrons with Fe atoms through coordinating bonds and weaken the adsorption of oxygen-containing intermediates on Fe sites. The above reverse effects are expected to result in strengthened Ni/O and weakened Fe/O bonds, thereby enhancing the catalytic activities of Ni sites and activating Fe sites. Density functional theory (DFT) calculation was used to further clarify the mechanism of OER performance improvement. To synthesize the FeNi- C_3N_4 -P catalyst, FeNi Prussian Blue Analogues (PBA) were first produced on a Ni foam substrate in the presence of C_3N_4 . The obtained material was then subjected to a high-temperature phosphating process. As expected, the resulting FeNi- C_3N_4 -P catalyst exhibited excellent OER activity with a small Tafel slope of 40.4 mV dec^{-1} , a low overpotential of 235 mV at 100 mA cm^{-2} and a remarkable stability. This work highlights the crucial role of the C_3N_4 substrate in enhancing the catalytic performance of both Ni and Fe sites in metal phosphides catalysts. It provides a new design strategy for developing high-performance OER catalysts.

2. Experimental section

2.1. Materials

Nickel foam (NF), copper foam (CF), nickel-iron foam (NIF), melamine, potassium ferricyanide (III) ($\text{K}_3\text{Fe}(\text{CN})_6$), citric acid, sodium hypophosphite (NaH_2PO_2), anhydrous ferric chloride, potassium hexacyanocobaltate (III) ($\text{K}_3\text{Co}(\text{CN})_6$), potassium hexacyanoferrate (II) ($\text{K}_4\text{Fe}(\text{CN})_6$), red phosphorus were purchased from Aladdin Industrial Corporation. All chemicals were used in their as-purchased form without any pre-treatment or modification.

2.2. Synthesis of C_3N_4

The C_3N_4 material was synthesized by subjecting melamine (5 g) to high temperature treatment in the absence of oxygen. Specifically, the melamine powder was placed in a porcelain boat and heated in a tube furnace under an argon atmosphere. The temperature was raised to 550°C at a heating rate of 5°C min^{-1} and maintained at this temperature for 4 h. Subsequently, the furnace was cooled down to room temperature, and the resulting C_3N_4 was taken out.

2.3. Synthesis of FeNi- C_3N_4 -P

The synthesis of the FeNi- C_3N_4 -P catalyst involved two steps: a hydrothermal reaction and a high-temperature phosphating process. A NF with dimensions of $2.0 \text{ cm} \times 2.5 \text{ cm}$ was cleaned by using sonication in 3 M HCl (30 min), acetone (8 min), ethanol, and deionized water (10 min) consecutively.

In the hydrothermal reaction step, a homogeneous mixture was first prepared by dispersing $\text{K}_3\text{Fe}(\text{CN})_6$ (1 mmol), C_3N_4 (92 mg), and citric acid (1 mmol) in 15 mL of deionized water through magnetic stirring at room temperature. The resulting mixture was then transferred into a 30 mL Teflon-lined autoclave containing the pretreated Ni foam. The autoclave was then sealed and maintained at 100°C for 3 h. The autoclave was cooled to room temperature, and the Ni foam was subsequently dried at 65°C for 4 h.

For the high-temperature phosphating step, the dried Ni foam (NF) was placed in a porcelain boat, and 500 mg of NaH_2PO_2 was put upstream in the same boat. The boat was then inserted into a tube furnace, and the temperature was gradually raised to 350°C at a heating rate of 5°C min^{-1} under an argon atmosphere. The furnace was kept at 350°C for 2 h before cooling down to room temperature. This process resulted in the FeNi- C_3N_4 -P catalyst. The sample of FeNi- C_3N_4 -P on the NF is 3.5 mg.

For comparison, a FeNi-P catalyst was prepared by using the same

procedure but without the addition of C_3N_4 . In addition, a FeNi- C_3N_4 catalyst was synthesized without the high-temperature phosphating step. The samples on the NF are 3.4 mg for FeNi-P and 5.6 mg for FeNi- C_3N_4 , respectively.

To load commercial catalysts such as IrO_2 and RuO_2 onto the Ni foam, the following method was used. Firstly, a mixed solution was prepared by mixing 240 μ L of ethanol, 60 μ L of Nafion (5 wt%), and 700 μ L of deionized water. Next, 25 mg of the commercial catalysts (RuO_2 or IrO_2) were added to the solution. The mixture was then dispersed by using sonication until a uniform ink was obtained. 150 μ L of the catalyst ink was dropped onto the Ni foam substrate. Afterward, the Ni foam with the catalyst ink was dried again in airflow to remove any remaining solvent. The resulting catalyst-loaded Ni foam had a mass of 3.1 mg for RuO_2 and 2.8 mg for IrO_2 , respectively.

2.4. Structural characterization

The crystal structures of the as-prepared catalysts were analyzed by using various characterization techniques. Powder X-ray diffraction (XRD) was carried out on a Bruker D8 Advance X-ray diffractometer using Cu K α radiation, operating at 40 kV and 40 mA. X-ray photoelectron spectroscopy (XPS) was performed on a Thermo Scientific K-Alpha XPS instrument. Transmission electron microscopy (TEM) and high-resolution transmission electron microscopy (HRTEM) were conducted using a FEI Tecnai G2 F30 microscope. Energy-dispersive X-ray spectroscopy (EDS) was performed alongside TEM to analyze the elemental composition of the catalyst materials. The exfoliation process of the sample from the NF foam involved ultrasonication. After exfoliation, the sample was dried at 60 °C using a vacuum oven. Once dried, the sample was ground into a powder form. To prepare for testing, the powdered sample was mixed with one hundred times its weight in KBr. The mixture was then pressed into a transparent sheet, which would be used for the FT-IR test. FT-IR measurement was performed on a Varian 800 FT-IR spectrometer at the wavenumber range of 4000 down to 400 cm^{-1} .

2.5. Electrochemical measurements

All electrochemical experiments were performed in a 1.0 M KOH electrolyte solution using an Autolab potentiostat/galvanostat (PGSTAT-302 N) workstation at room temperature. A typical three-electrode cell system was used, consisting of the catalyst working electrode, a graphite counter electrode, and a Hg/HgO reference electrode. Before each measurement, the KOH electrolyte was purged with high-purity argon (Ar) gas for at least 30 min to remove any dissolved oxygen. Prior to the OER measurements, 20 cycles of cyclic voltammetry (CV) tests were performed to activate the catalyst. Linear sweep voltammetry (LSV) curves were conducted in 1.0 M KOH solution with a scan rate of 5 $mV s^{-1}$ to study the oxygen evolution reaction (OER). All potentials applied in the experiments were referenced to the reversible hydrogen electrode (RHE) using the following equation: E (V vs. RHE) = E (V vs. Hg/HgO) + 0.0591 pH + 0.098.

The stability of the catalyst was assessed by performing successive potential scanning, chronoamperometry, and chronopotentiometry measurements. To evaluate the electrochemical active surface areas (ECSAs) of the catalyst, CVs were conducted at different scanning rates (20 $mV s^{-1}$, 40 $mV s^{-1}$, 60 $mV s^{-1}$, 80 $mV s^{-1}$, and 100 $mV s^{-1}$). The electrochemical double-layer capacitance (C_{dl}) was calculated from the CV data. For further characterization, electrochemical impedance spectroscopy (EIS) measurements were performed in the frequency range of 0.01–105 Hz using an AC amplitude of 5 mV.

2.6. DFT calculations

The Vienna ab-initio simulation package (VASP) was used for the spin-polarized density functional theory (DFT) calculations [33,34]. The

projector augmented wave (PAW) method with a cutoff energy of 400 eV was employed [34], and the Perdew-Burke-Ernzerhof (PBE) functional was used in the DFT calculations [35]. To consider van der Waals interactions, the DFT-D3 method was used [36]. The heterojunction model consisted of a cleaved C_3N_4 (111) facet and FeNiP (111) facet, with a vacuum layer of 20 Å. The bulk phase of C_3N_4 was simulated by fixing the half layer. To ensure convergence, all models were fully relaxed with an energy convergence criterion of 10^{-5} eV and a force convergence criterion of 0.02 eV/Å. The Brillouin zone integration was performed using a Monkhorst-Pack k-point mesh of the Γ point.

The adsorption energy (E_{ads}) in the DFT calculation was calculated using the following formula 1:

$$E_{ads} = E_{total} - E_{substrate} - E_{adsorbate} \quad (1)$$

Where E_{total} , $E_{substrate}$ and $E_{adsorbate}$ represent the energy of adsorption structure, substrate and adsorbate, respectively. The free energies have been calculated using the following formula 2:

$$G = E_{DFT} + ZPE - TS \quad (2)$$

The G, E_{DFT} , ZPE and TS represent the free energy, energy from DFT calculations, zero-point energy and entropic contributions, respectively.

3. Results and discussion

3.1. OER mechanism analysis

We firstly performed DFT to investigate the catalytic activity of Ni sites and Fe sites in FeNi-P, as well as the influence of C_3N_4 on the electron configuration of these catalytic active sites. DFT calculation were carried out on the (111) plane of FeNi-P and FeNi- C_3N_4 -P catalysts (Fig. S1). Previous studies have established that the metal atoms, Fe and Ni, are typically regarded as the catalytic active sites [22,24,37]. These active sites form bonds with the OER intermediates through bridge (two points) or hole (three points) configurations [14,38]. To evaluate the catalytic activity, we specifically considered the surface Ni sites (Ni1, Ni2, Ni3) and Fe sites (Fe1, Fe2) for our calculations. The positions of these Ni and Fe sites in both FeNi-P and FeNi- C_3N_4 -P catalysts are depicted in Fig. 1A. It should be noted that the adsorption of intermediates may also involve the neighboring Ni, Fe, and P atoms.

First, we performed Bader analysis to gain insights into the charge transfer behavior between C_3N_4 and FeNiP. As shown in Fig. 1B (left) and Table S1, the total charge donation from FeNi-P to C_3N_4 was 8.031 e, resulting in significant charge redistribution on Fe-Ni phosphide. Detailly, the Bader charge of P and Ni decreases from + 0.469 e to + 0.167 e and from - 0.078 e to - 0.156 e after the addition of C_3N_4 , respectively. In addition, the Bader charges of C and N were measured to be - 1.008 e and + 1.002 e, respectively (here, the "-" symbol indicates accepted charge, while the "+" symbol denotes donated charge) (Fig. 1B right). The decrease in Bader charges of P and Ni atoms after C_3N_4 incorporation can be attributed to the electronegativity difference of P (2.19), Ni (1.91), and N (3.04). The increased electron-donation of Ni results in an enhanced adsorption strength of oxygen-containing intermediates at the Ni sites. Interestingly, although Fe has a lower electronegativity of 1.83, its Bader charge actually changes from - 0.391 e to - 0.359 e, indicating a net decrease in the electron donation of Fe atoms in FeNi- C_3N_4 -P. This abnormal change in Bader's charge is mainly due to the strong coordination between Fe and N atoms at the interface [22]. We believe that these coordination bonds weaken the interaction between Fe and oxygen-containing intermediates, thus promoting the OER process at the Fe site.

The electron structures of FeNi-P and FeNi- C_3N_4 -P were then examined through density of states (DOS) analysis to understand the contributions of C_3N_4 . After the incorporation of C_3N_4 , the DOS shape and spread width of P, Fe, Ni and the total changed significantly (shown in Fig. S2 and Fig. S3). It can be observed in Fig. 1C that, with the

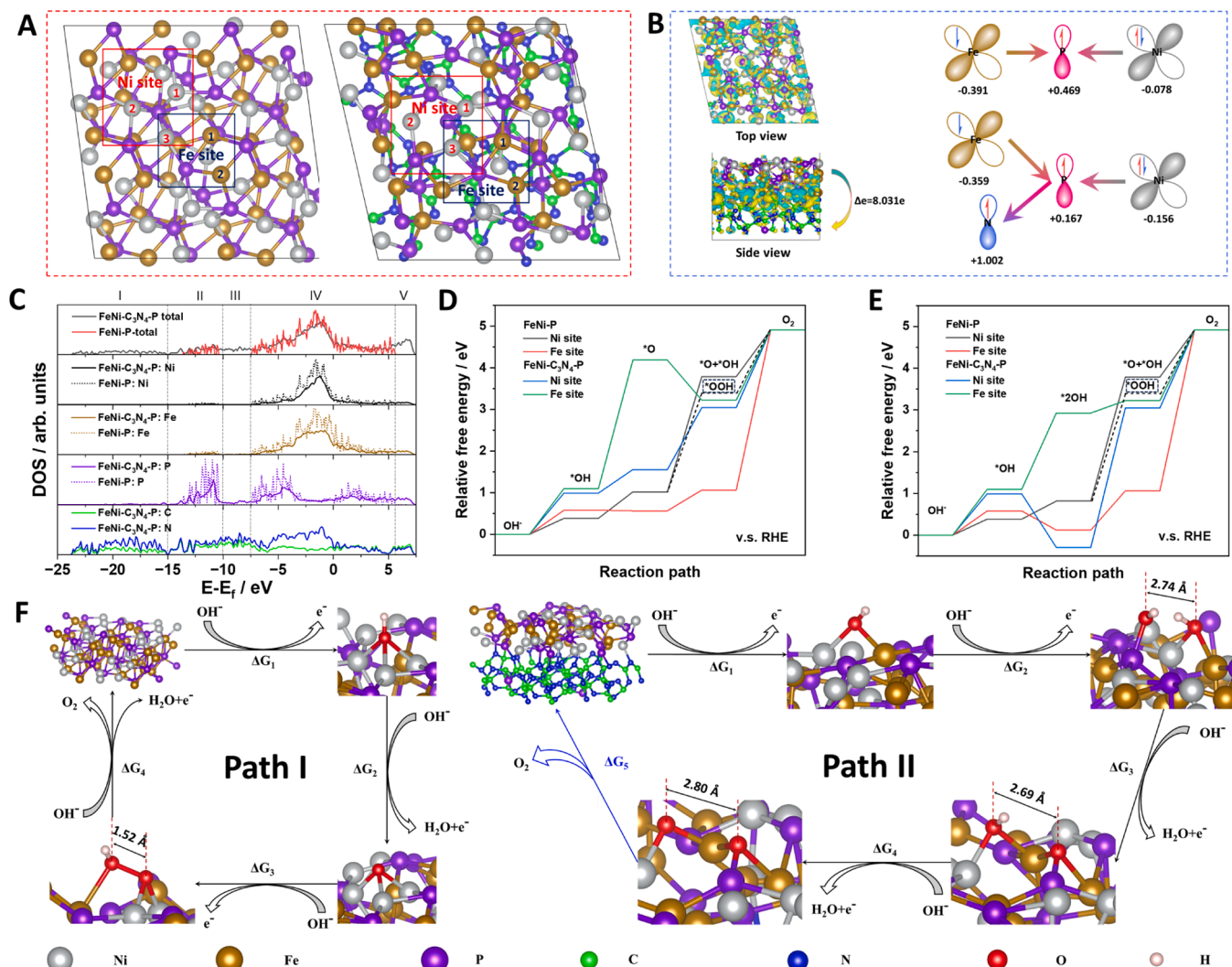


Fig. 1. Theoretical OER mechanism and catalytic structure of Fe–Ni dual sites in FeNi-P and FeNi-C₃N₄-P. (A) The catalytic Fe site and Ni site on FeNi-P and FeNi-C₃N₄-P. (B) The geometric structure and corresponding electron density difference of FeNi-C₃N₄-P. Yellow and cyan areas represent the electron accumulation and depletion, respectively. (C) DOS comparison of FeNi-P and FeNi-C₃N₄-P, and the individual DOS of C, N, Fe, Ni, P element. (D) and (E) The relative free energy diagrams for OER process on Fe site and Ni site in FeNi-P and FeNi-C₃N₄-P through conventional two paths. In Path II, the step of $^*O + ^*OH \rightarrow 2^*O \rightarrow O_2$ was simplified as $^*O + ^*OH \rightarrow O_2$ because that the $2^*O \rightarrow O_2$ is a chemical process without electron transfer. (F) The adsorption configurations of OER intermediates and the OER processes. The Ni site in FeNi-P follows the Path I, the Fe site in FeNi-C₃N₄-P follows the Path II.

introduction of C₃N₄, FeNi-C₃N₄-P obtains a continuous DOS, which can be divided into five regions. Zones I (−25 eV~−15 eV), III (−10 eV~−7.5 eV) and V (+6 eV~+7.5 eV) are derived from C, N and P, respectively, while Zones II (−15 eV~−10 eV) and IV (−7.5 eV~+6 eV) are derived from P and metal (Fe, Ni), respectively. In contrast, only two separate regions, II and IV, were observed in FeNi-P. This modulation in DOS may cause significant changes in adsorption/desorption behavior and contribute to outstanding charge transfer capabilities [15,39]. The *d*-band centers of Ni and Fe atoms were further analyzed. The results show that the *d*-band centers of Ni and Fe atoms increased by 0.2 eV~0.4 eV after the addition of C₃N₄. This indicates that FeNi-C₃N₄-P has stronger adsorptions of oxygen-containing OER intermediates than FeNi-P.

Finally, the catalytic activity of Fe and Ni sites in FeNi-P and FeNi-C₃N₄-P was evaluated by comparing the Gibbs free energies of intermediates (*OH , *O and *OOH) involved in conventional OER processes. In FeNi-P, due to the weak adsorption of *OOH at the Ni site, *OOH formation becomes the rate-determining step (RDS) with an energy barrier of 2.37 eV (Fig. 1D). The adsorption configuration of OER intermediates at the Ni site of FeNi-P is shown in Fig. S4. *OOH

configuration shows one O-Fe bond, two O-Ni bonds, and one 1.52 Å O-O bond. Therefore, OER at the Ni site of FeNi-P follows the $^*OH \rightarrow ^*O \rightarrow ^*OOH \rightarrow O_2$ path (Fig. 1F, path I). However, with the addition of C₃N₄, the adsorption strength of *OOH at Ni site was enhanced, resulting in spontaneous cleavage to *O and *OH . As shown in Fig. S5, the *OOH configuration on Ni changes to one O-Fe bond, four O-Ni bonds and an O-O distance of 2.85 Å (without O-O bond), which is almost twice the O-O distance in FeNi-P. Therefore, the OER process at the Ni site of FeNi-C₃N₄-P changes to $^*OH \rightarrow ^*O \rightarrow ^*O + ^*OH \rightarrow 2^*O \rightarrow O_2$ path, where RDS is the step of $^*O + ^*OH \rightarrow 2^*O \rightarrow O_2$ and the energy barrier is 1.88 V (Fig. 1E, F Path II).

The situation is quite different at the Fe site compared to the Ni site. Due to its high affinity for oxygen, the Fe site in FeNi-P has a strong adsorption for oxygen atoms, and the adsorbed *OOH is spontaneously decomposed into *O and *OH (Fig. 1E). This suggests that the OER process at the Fe site follows a direct O₂ mechanism. In this mechanism, two *OH bind to adjacent catalytic sites, undergo two coupled electron-proton transfer steps to form two *O intermediates, and then undergo a pure chemical step to produce O₂ [23]. At the Fe site of FeNi-P, the $^*O + ^*OH$ configuration contains two O-Fe bonds, four O-Ni bonds and

an O-O distance of 2.81 Å (without O-O bond)(Fig. S6). The RDS of this process is the conversion of $\ast\text{O} + \ast\text{OH}$ to O_2 , and the energy barrier is 3.85 eV. Importantly, the introduction of C_3N_4 led to a significant change in adsorption behavior at the Fe site, which altered the RDS process. In FeNi- C_3N_4 -P, the $\ast\text{O} + \ast\text{OH}$ configuration at the Fe site consists of one O-Ni bond, three O-Fe bonds, one O-P bond and an O-O distance of 2.69 Å (without O-O bond)(Fig. 1F Path II, Fig. S7). The change in configuration, coupled with the N-coordination effect described above, leads to a weaker adsorption strength at the Fe site ($\Delta E = -2.16$ eV). In addition, with the addition of C_3N_4 , the $\ast\text{O}$ configuration at the Fe site changes from one O-Ni and two O-Fe bonds to one O-P and two O-Fe bonds, further reducing the $\ast\text{O}$ adsorption strength ($\Delta E = 3.62$ eV). Similarly, the adsorption of $2 \ast\text{OH}$ is weakened ($\Delta E = 2.80$ eV), from two O-Fe and three O-Ni bonds to one O-P, one O-Fe and one O-Ni bond. Thus, in FeNi- C_3N_4 -P, OER follows the $\ast\text{OH} \rightarrow 2 \ast\text{OH} \rightarrow \ast\text{O} + \ast\text{OH} \rightarrow 2 \ast\text{O} \rightarrow \text{O}_2$ pathway, where RDS is the step of $\ast\text{OH} \rightarrow 2 \ast\text{OH}$ and the energy barrier is 1.82 eV. In summary, the incorporation of C_3N_4 in FeNi-P catalyst significantly changed the adsorption behavior and catalytic activity of Fe and Ni sites in OER process. The enhanced adsorption of $\ast\text{OOH}$ at the Ni site in FeNi- C_3N_4 -P led to spontaneous cleavage to $\ast\text{O}$ and $\ast\text{OH}$, thereby altering the OER pathway and reducing the RDS barrier by 0.49 eV (from 2.37 eV to 1.88 eV) (Table S3). The strong adsorption of Fe to oxygen-containing intermediates in FeNi-P promotes the spontaneous cleavage of $\ast\text{OOH}$ to $\ast\text{O}$ and $\ast\text{OH}$. However, the incorporation of C_3N_4 weakened the adsorption strength, activated the Fe site, and achieved an optimized RDS process with an energy barrier of 1.82 eV. Thus, in FeNi-P, OER occurs mainly at the Ni site through path I, while in FeNi- C_3N_4 -P, OER occurs mainly at the Fe site through path II and partly at the Ni site. This indicated that C_3N_4 enhanced the catalytic activity of Ni site and activated Fe site, making Fe the main active site of OER process. These findings provide valuable insights into the catalytic mechanism and potential applications of FeNi- C_3N_4 -P as a highly efficient OER catalyst.

3.2. Synthesis and structural characterization of FeNi- C_3N_4 -P catalyst

The synthesis process of FeNi- C_3N_4 -P is shown in Fig. 2 A. FeNi PBA was first grown on the surface of NF by hydrothermal method, and then converted into metal phosphide by high temperature treatment with NaH_2PO_2 . In the first step, FeNi PBA was prepared on the NF surface by hydrothermal method at 100 °C and 3 h in the presence of C_3N_4 using only $\text{K}_3[\text{Fe}(\text{CN})_6]$. The equilibrium electrode potential (E_{eq}^0) of Fe

$(\text{CN})_6^{3-}/\text{Fe}(\text{CN})_6^{4-}$ is 0.36 V, which is much higher than that of Ni^{2+}/Ni (−0.246 V). The metal Ni can be oxidized by $\text{Fe}(\text{CN})_6^{3-}$ and changes into Ni^{2+} . Thus, in the hydrothermal process, the NF surface dissolves and reacted with $\text{K}_3[\text{Fe}(\text{CN})_6]$ to form FeNi PBA. Ni ions were derived from the NF surface, allowing FeNi PBA to grow firmly on the NF skeleton. The formation of FeNi-PBA was confirmed by XRD pattern (Fig. S8). In the second step, NF-supported FeNi PBA/ C_3N_4 composites reacted with NaH_2PO_2 at 350 °C for 2 h. This high-temperature treatment resulted in the conversion of FeNi PBA to metal phosphide [40].

Firstly, the structure of the catalysts were characterized by X-ray diffraction (XRD). The XRD patterns shown in Figs. 2B and 2C present the crystallinity of the as-prepared C_3N_4 and FeNi- C_3N_4 -P. For C_3N_4 , the peaks at 25.96° and 28.31° can be attributed to the diffraction of C_3N_4 (pdf: 50-1249). The peak at 12.88° corresponds to the (002) diffraction of the interlayer repeated tri-triazine units [41]. In addition, weak peaks at 17.72° and 21.48° indicated the existence graphitized carbon nitride [41]. For FeNi- C_3N_4 -P, the sharp peaks at 44.45°, 51.85° and 76.38° can be assigned to the metal nickel of the NF skeleton (pdf: 65-2865). The relatively weaker peaks at 40.71°, 47.33° and 54.10° correspond to the diffraction pattern of metal phosphides, demonstrating a close match with the (111), (210) and (300) planes of Ni_2P (pdf: 65-1989) and Fe_2P (pdf: 51-0943). It has been reported that these two metal phosphides often co-exist due to their highly similar crystal parameters [42, 43].

The growth and morphology of the FeNi- C_3N_4 -P catalyst on the NF were characterized by scanning electron microscopy (SEM) and transmission electron microscopy (TEM). The SEM images in Fig. 3 A show that the surface of NF is covered with a layer of high-density products. The inset picture in Fig. 3 A, with a larger magnification, reveals that these products have a cubic shape, similar to the typical morphology of PBA [44].

To further analyze the fine structure of the products, the exfoliated samples were analyzed by TEM. In the TEM images of Fig. 3B and Fig. 3C, the lattice spacing of 3.4 Å and 3.1 Å is in good agreement with the XRD diffraction peaks of C_3N_4 . The lattice spacing of 2.2 Å, 1.9 Å, and 1.7 Å corresponds to the (111), (210), and (300) planes of Ni_2P or Fe_2P , respectively, which is consistent with the XRD diffractions of metal phosphide. TEM-EDS analysis (Fig. 3D) confirms the presence of C, N, Fe, Ni, and P elements in the catalyst. Elemental mapping analysis (Fig. 3E-J) shows that Fe, Ni, C, N and P are highly distributed throughout the catalyst.

The atomic ratio of Fe/Ni/P is determined to be 4.8/4.4/5.1. Based

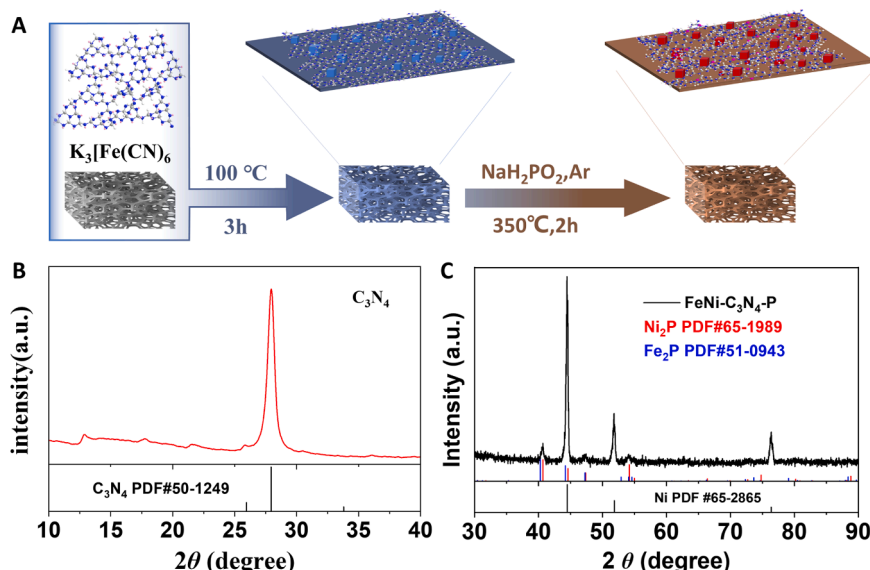


Fig. 2. (A) Schematic illustration for formation process of FeNi- C_3N_4 -P. XRD of as-prepared (B) C_3N_4 and (C) FeNi- C_3N_4 -P.

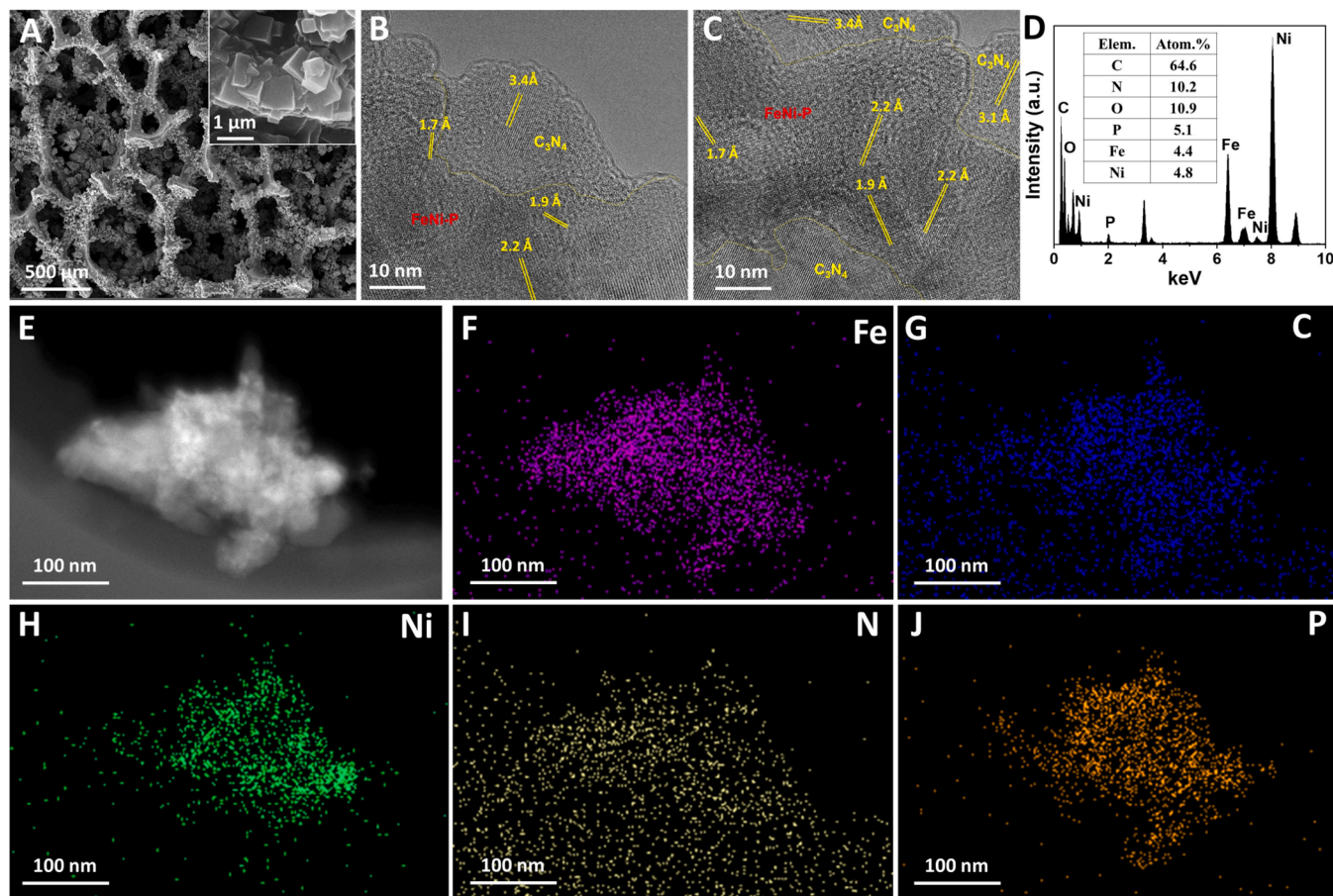


Fig. 3. (A) SEM image of FeNi-C₃N₄-P. The inset is the SEM image with larger magnification. (B) and (C) HRTEM images of FeNi-C₃N₄-P. (D) TEM-EDS spectra of FeNi-C₃N₄-P. (E) STEM image and the corresponding elemental mapping of (F) Fe, (G) C, (H) Ni, (I) N and (J) P.

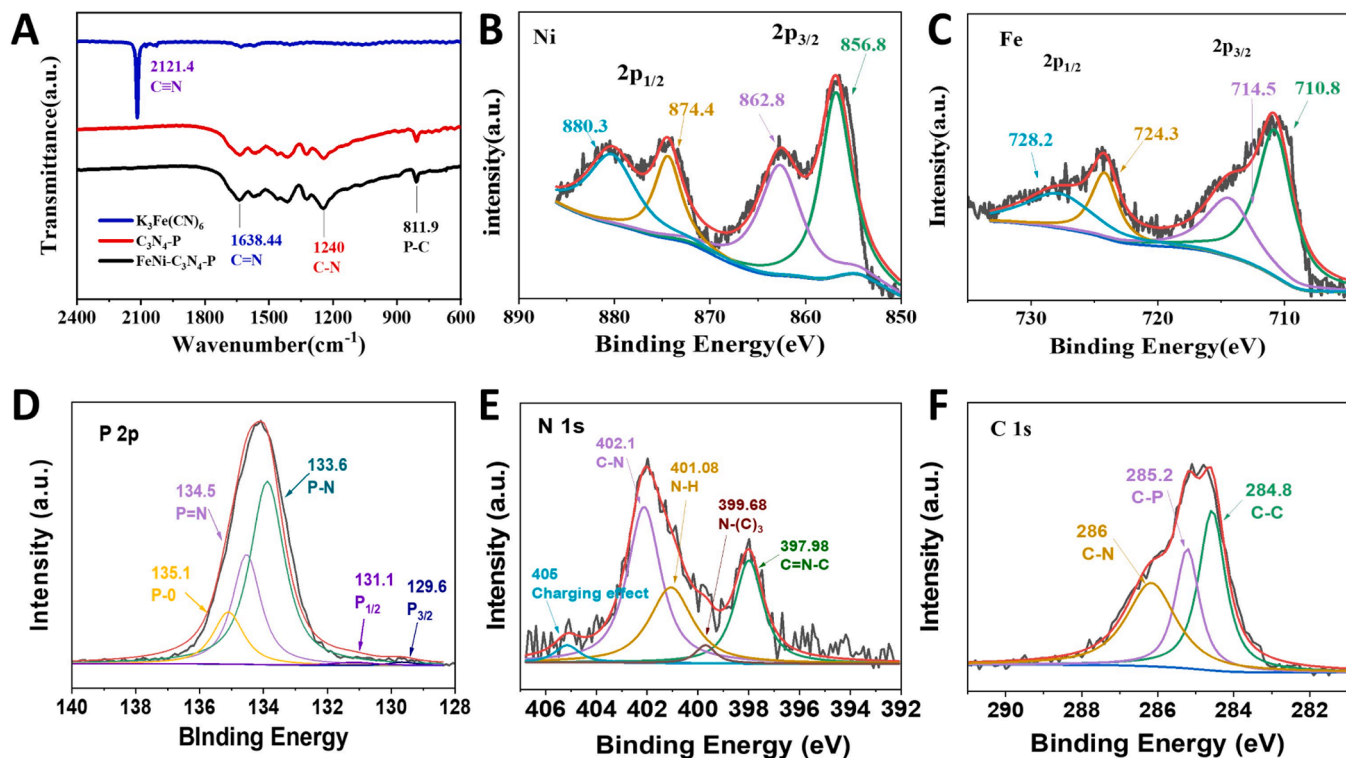


Fig. 4. (A) FT-IR spectrum of K₃Fe(CN)₆, C₃N₄-P and FeNi-C₃N₄-P. High-resolution XPS spectra of (B) Ni, (C) Fe, (D) P, (E) N and (F) C of FeNi-C₃N₄-P.

on the comparison of atomic ratios with Ni_2P and Fe_2P , we believe that some P atoms have been doped into the C_3N_4 , based on the atomic ratio compared to [40]. Although the heterostructure of Ni_2P - Fe_2P has been reported previously [16,45], distinguishing between Ni_2P and Fe_2P is still challenging due to the highly similar structural parameters. Considering that the catalyst was prepared by FeNi-PBA, in which Fe and Ni are highly atomically dispersed, we believe that the bimetallic phosphide has a homogeneous structure. Therefore, it is more appropriate to describe this bimetallic phosphide as FeNi- C_3N_4 -P. For the following comparisons, the unphosphating product (FeNi- C_3N_4) and C_3N_4 absent sample (FeNi-P) were also prepared through the same method (Fig. S9 and Fig. S10).

The molecular structure and changes during the synthesis were characterized by FT-IR spectra. It can be observed in Fig. 4 A that the CN bond at 2121.4 cm^{-1} , present in $\text{K}_3\text{Fe}(\text{CN})_6$, has disappeared in FeNi- C_3N_4 -P, indicating that the CN bond has been completely broken or removed. In addition, peaks corresponding to $\text{C}=\text{N}$ (1638.44 cm^{-1}), C-N (1240 cm^{-1}), and P-C (811.9 cm^{-1}) appear in FeNi- C_3N_4 -P, suggesting that P has entered the C_3N_4 structure.

The chemical composition and state were analyzed by X-ray photoelectron spectroscopy (XPS). The major peaks of 856.8 eV and 874.4 eV in Ni spectra correspond to $\text{Ni } 2p_{3/2}$ and $\text{Ni } 2p_{1/2}$ of Ni^{2+} , respectively, accompanied with satellites at 862.8 eV and 880.3 eV (Fig. 5B) [46]. The broad peaks of 710.8 eV and 724.3 eV in Fe spectra are $\text{Fe } 2p_{3/2}$ and $\text{Fe } 2p_{1/2}$ of Fe^{2+} , respectively, and the satellites located at 714.5 eV and 728.2 eV (Fig. 5C) [42]. The P spectra can be deconvoluted into P-N (133.6 eV) and P = N (134.5 eV) [47]. The peaks at 130 eV were deconvoluted into $\text{P}_{3/2}$ and $\text{P}_{1/2}$ at 129.6 eV and 131.1 eV , corresponding to metal phosphide. There might be some oxides or phosphate on the sample surface due to the oxidation in air. A XPS peak was observed at 135.1 eV , which can be assigned to P-O bond, indicating oxidation of the sample surface in the air. The peaks of 397.98 eV ,

399.68 eV , 401.08 eV , and 402.1 eV in N spectra correspond to $\text{C}=\text{N}$ -C, $\text{N}(\text{C})_3$, N-H, and C-N bonds, respectively [40,46]. The peak of the C 1s spectrum can be deconvoluted into standard C-C (284.8 eV), C-P (285.2 eV), and C-N (286 eV) [46,48]. The position changes of P, Ni, and Fe in FeNi-P and FeNi- C_3N_4 -P clearly indicate that the modulation effect of C_3N_4 is significant (Fig. S11). These results indicated that a C_3N_4 decorated Fe/Ni phosphide catalyst has been successfully fabricated on the Ni NF surface.

3.3. OER performance of FeNi- C_3N_4 -P catalyst

The electrocatalytic performance of FeNi- C_3N_4 -P was evaluated in a conventional three-electrode system with HgO as reference electrode and a graphite rod as the counter electrode. For comparison, commercial benchmark catalysts of RuO_2 and IrO_2 were loaded onto NF and tested under the same conditions. As depicted in Fig. 5 A, FeNi- C_3N_4 exhibited lower performance compared to commercial RuO_2 and IrO_2 catalysts. However, the catalytic performance of FeNi-P was higher than that of FeNi- C_3N_4 and similar to that of IrO_2 , indicating that the metal phosphide has superior activity [10]. Interestingly, FeNi- C_3N_4 -P demonstrated the highest performance, as evidenced by its lowest onset potential and highest current density. This indicates that the introduction of C_3N_4 greatly improves the electrocatalytic activity of metal phosphide. In bidirectional scanning, the current density tends to overlap at high overpotential, indicating that a similar electrochemical process, that is, oxygen evolution, occurs during the bidirectional scanning at the high potential region. However, significant differences can be observed at low potential. For instance, in the case of FeNi- C_3N_4 -P, there is a distinct metal oxidation peak in the forward scan of $1.3\text{--}1.45\text{ V}$. In the back scan, there is a clear metal reduction peak. Notably, the reduction peak spans a wider range of potential. In order to minimize the influence of metal oxidation behavior [38], the

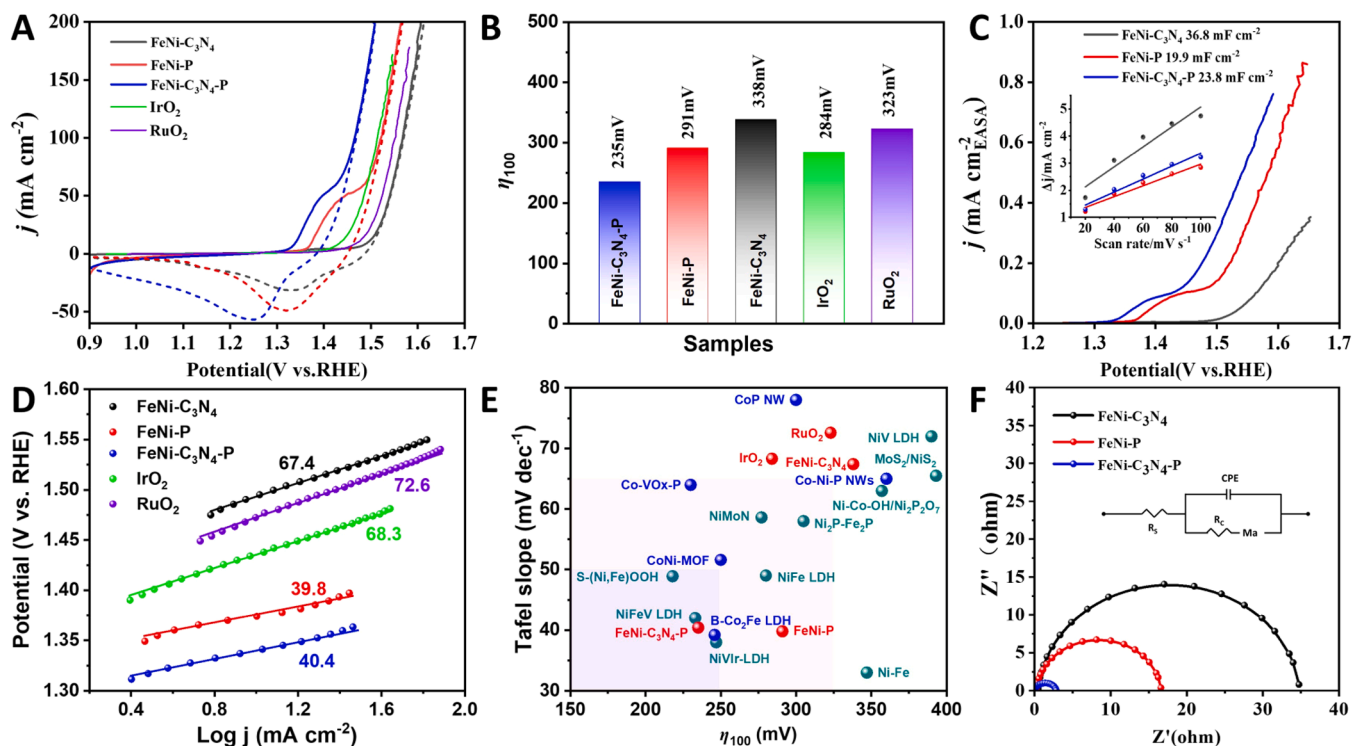


Fig. 5. (A) Polarization curves of IrO_2 , RuO_2 , FeNi-P, FeNi- C_3N_4 , and FeNi- C_3N_4 -P. The solid lines present the forward scanning and the short dashes present the backward scanning. (B) Overpotentials for 100 mA cm^{-2} of IrO_2 , RuO_2 , FeNi-P, FeNi- C_3N_4 and FeNi- C_3N_4 -P. (C) Polarization curves of FeNi-P, FeNi- C_3N_4 normalized by the C_{dl} . Inset is the C_{dl} of the samples obtained from CV curves in a non-Faraday region. (D) Tafel slopes of IrO_2 , RuO_2 , FeNi-P, FeNi- C_3N_4 and FeNi- C_3N_4 -P. (E) Comparison of FeNi- C_3N_4 with the reported catalysts [16,38,59–70], regarding to Tafel slopes and overpotentials at 100 mA cm^{-2} . (F) EIS spectra of FeNi-P, FeNi- C_3N_4 and FeNi- C_3N_4 -P.

overpotentials at a higher current density of 100 mA cm^{-2} (η_{100}) was selected for further evaluation of the catalytic performances. As shown in Fig. 5B, the η_{100} of FeNi-C₃N₄-P was 235 mV, which is significantly lower than those of FeNi-P (291 mV) and FeNi-C₃N₄ (338 mV). In addition, the performance of FeNi-C₃N₄-P surpasses other reported transition metal phosphides, such as FeCoNi-P (η_{100} = 289 mV) [44], CoP nanorod (η_{10} = 320 mV) [49], V-CoP (η_{10} = 267 mV) [50], NiCoP/C nano-box (η_{10} = 330 mV) [51] and Fe-Co-P nano-box (η_{10} = 269 mV) [52]. To our knowledge, the FeNi-C₃N₄-P catalyst described here is the highest performing transition metal phosphides reported to date [21,53,54]. To better understand the underlying reason behind the improvement of OER performance, the electrochemical active surface area (EASA) of different catalysts were evaluated and compared. EASA was quantified by the electrochemical double-layer capacitance (C_{dl}), which was determined by cyclic voltammetry measurements in the non-Faraday region (Fig. S12) [55]. The C_{dl} value of FeNi-C₃N₄ is largest (36.8 mF cm^{-2}), 1.5 times that of FeNi-C₃N₄-P (23.8 mF cm^{-2}), indicating that the phosphating process may cause slight loss of pore structure or pore-surface properties [56]. Despite this, the EASA of FeNi-C₃N₄-P was still 20 % larger than that of FeNi-P, suggesting that the presence of C₃N₄ could improve the accessibility of the catalytic sites. Similar observations have been made in other catalysts using carbonaceous substrates [45,57]. To further evaluate the real activity of the catalytic sites, the OER current densities in the forward scanning direction (as shown in Fig. 5A) were normalized by EASA [58]. The results, depicted in Fig. 5C, demonstrated that FeNi-C₃N₄-P exhibited higher performance compared to FeNi-P. The Tafel slopes were then tested and used to assess the change in potential with the current density [9]. As shown in Fig. 5D, the Tafel slope of FeNi-C₃N₄-P is relatively small, which is 40.4 mV dec^{-1} , similar to that of FeNi-P (39.8 mV dec^{-1}). However, it was significantly lower than those of FeNi-C₃N₄ (67.4 mV dec^{-1}), IrO₂ (68.3 mV dec^{-1}), and RuO₂ (72.6 mV dec^{-1}). This indicates that the FeNi-C₃N₄-P catalyst exhibits obvious intrinsic activity, in which a small

overpotential increment is required to achieve a rapid increase in the current density. In Fig. 5E, FeNi-C₃N₄-P outperforms recently reported transition metal-based OER catalysts, demonstrated in terms of overpotential and Tafel slopes. These results further highlight the outstanding performance of FeNi-C₃N₄-P compared to other catalysts in the literature. To further investigate the contribution of charge transfer to the enhancement of catalytic activity, the electrochemical impedance spectroscopy (EIS) test was then performed [55]. As shown in Fig. 5F, the EIS spectra of the three samples are approximately semicircular but with different diameters. The semicircle diameter of the FeNi-P is half that of FeNi-C₃N₄, indicating good conductivity. This can be attributed to the metal-like nature of phosphides. Interestingly, FeNi-C₃N₄-P has the smallest semicircle diameter, suggesting the lowest charge transfer resistance. This indicates that FeNi-C₃N₄-P has better conductivity than FeNi-P. These findings are consistent with previous research that the presence of carbon substrates can enhance the electrical conductivity of metal phosphide [51].

3.4. Stability test of FeNi-C₃N₄-P catalyst

To evaluate the stability of the FeNi-C₃N₄-P catalyst, the successive potential scanning, chronoamperometry, and chronopotentiometry measurements were performed. First, the potential was forward scanned 5000 cycles and the polarization curves were tested and recorded every 1000 cycles. Fig. 6A shows the polarization curves obtained during this process. It can be observed that the polarization curves showed neglectable changes after 3000 cycles, indicating good stability, and the metal oxidation peak at 1.4 V increases slightly after 5000 cycles. In the chronoamperometry test, the catalyst was first tested at an overpotential of 245 mV, and after 55 h, the current density obtained was 95.8 % of the initial value (as shown in Fig. 6B). Then tested at a higher overpotential of 320 mV the current density retained 98 % of the initial value after 28 h. The chronoamperometry test was compared with the recently

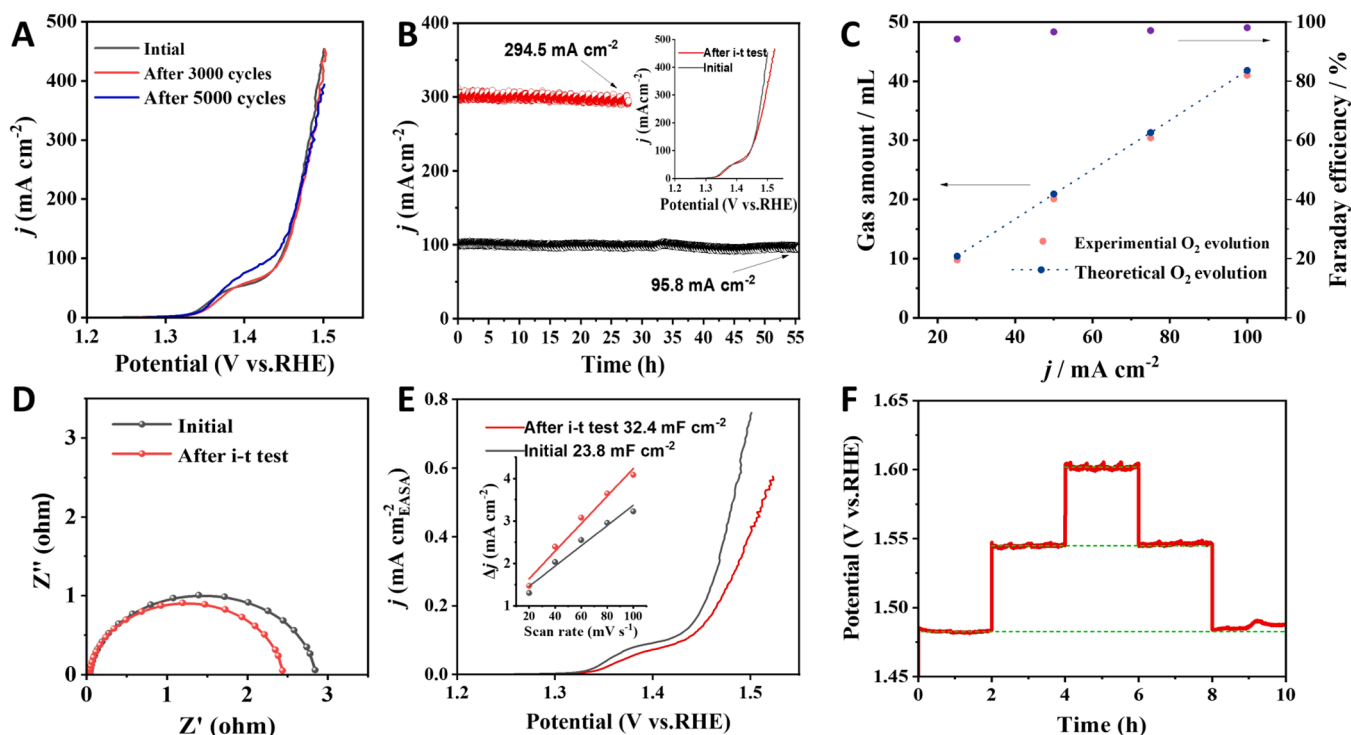


Fig. 6. The durability test of FeNi-C₃N₄-P catalyst. (A) Comparison of polarization curves, initial, after 3000 cycles and 5000 cycles. (B) i-t chronoamperometric tests for FeNi-C₃N₄-P at overpotentials of 245 mV and 320 mV for 28 h and 55 h in turn. Inset is the comparison of polarization curves of FeNi-C₃N₄-P after i-t test. (C) Gas collection test of FeNi-C₃N₄-P at 25 mA cm⁻², 50 mA cm⁻², 75 mA cm⁻² and 100 mA cm⁻². (D) Nyquist plots before and after the i-t test. (E) Polarization curves normalized by the C_{dl} . Inset is the C_{dl} of the sample obtained from CV curves in a non-Faraday region. (F) Chronopotentiometry tests at 100 mA cm⁻², 300 mA cm⁻², 450 mA cm⁻², 300 mA cm⁻² and 100 mA cm⁻².

reported catalysts in Table S4. Polarization curves were recorded after the chronoamperometry test. The potentials required to achieve the current densities of 200 mA cm^{-2} and 300 mA cm^{-2} increased by only 8 mV and 10 mV, respectively. These results indicate that the performance remained stable even at higher current densities (as shown in the inset in Fig. 6B). In addition, a gas collection test was performed at different current densities of 25 mA cm^{-2} , 50 mA cm^{-2} , 75 mA cm^{-2} , and 100 mA cm^{-2} . The Faraday efficiency, the efficiency of converting electrical energy into oxygen are all higher than 90 % and with the increase of current density, Faraday efficiency approaches 100 % (as shown in Fig. 6C). The EIS spectra shows that the charge transfer process was slightly enhanced after chronoamperometry test, as depicted in Fig. 6D. At the same time, the EASA of the catalyst increased by 33.3 % after the chronoamperometry test. This increase can be attributed to the "rinsing effect" of oxygen releasing [39]. Correspondingly, the current density normalized by EASA slightly decreased (as shown in Fig. 6E). Finally, a chronopotentiometry test was further performed at different current densities of 100 mA cm^{-2} , 300 mA cm^{-2} , 450 mA cm^{-2} , 300 mA cm^{-2} , and 100 mA cm^{-2} (each step lasted 2 h). Fig. 6F shows that the potential remained much more stable compared to general catalysts [39]. Importantly, at the same current density, the potential of the right side platform is almost the same as that on the left side. This exceptional stability can be attributed to the advanced structure inherited from the metal organic frames [44].

After the stability test of the chronoamperometric test, the catalyst was characterized by SEM, XRD, XPS, and TEM. The results indicate that the catalyst's structure, as well as the key phases and elemental dispersion, remained almost unchanged. The SEM image in Fig. 7A and

Fig. S13 revealed that the catalyst still maintained its cubic shape. As depicted in Fig. 7B, the (111) and (210) planes of Ni_2P or Fe_2P can also be observed in XRD pattern, which locates at 40.71° and 47.33° , respectively. The XPS spectra of Ni did not change significantly (Fig. 7C), indicating that the chemical state of nickel remained relatively stable. Comparing the XPS spectra of the catalyst before and after the stability test, it can be seen that the relative content of oxygen increased from 10.2 % to 19.8 % (Fig. 7D). This increase in oxygen content can be attributed to the surface oxidation [52]. TEM analysis showed that the elements of Fe, Ni, C, N, P, and O were still highly dispersed on the catalyst (Fig. 7E-J).

To understand the factors affecting the catalytic performance, the composition and synthesis conditions of the catalysts were studied. It can be seen from Fig. 8A that the catalysts on Fe foam and Cu foam exhibited poor catalytic activity due to the lack of Ni. Although various Fe_2P -containing catalysts such as $\text{Ni}_2\text{P-Fe}_2\text{P}$ [16], $\text{Co}_2\text{P @ NC-Fe}_2\text{P}$ [71], $\text{Co}_x\text{P-Fe}_2\text{P}$ [72], Co-doped Fe_2P [73], $\text{Ni}_2\text{P/Fe}_2\text{P}$ [45] and Ni-Fe phosphide [74] have been reported in previous study and shown good OER performance. However, pure Fe phosphides are generally considered to be a poor OER catalyst [75]. The catalysts on Ni foam and FeNi foam displayed similar performances, suggesting that their composition was the determining factor. This finding is consistent with previous studies in the field [16,45]. Fig. 8B compared the influence of various precursors of FeCl_3 , $\text{K}_3\text{Fe}(\text{CN})_6$, $\text{K}_4\text{Fe}(\text{CN})_6$, and $\text{K}_3\text{Co}(\text{CN})_6$ on catalytic performance. The catalyst synthesized with FeCl_3 as the precursor was not able to form the desired MOF structure, so the catalytic performance was poor. Similarly, the $\text{K}_3\text{Co}(\text{CN})_6\text{-C}_3\text{N}_4\text{-P}$ catalyst showed poor performance due to the lack of Fe. For the $\text{K}_4\text{Fe}(\text{CN})_6\text{-C}_3\text{N}_4\text{-P}$ catalyst, K_4Fe

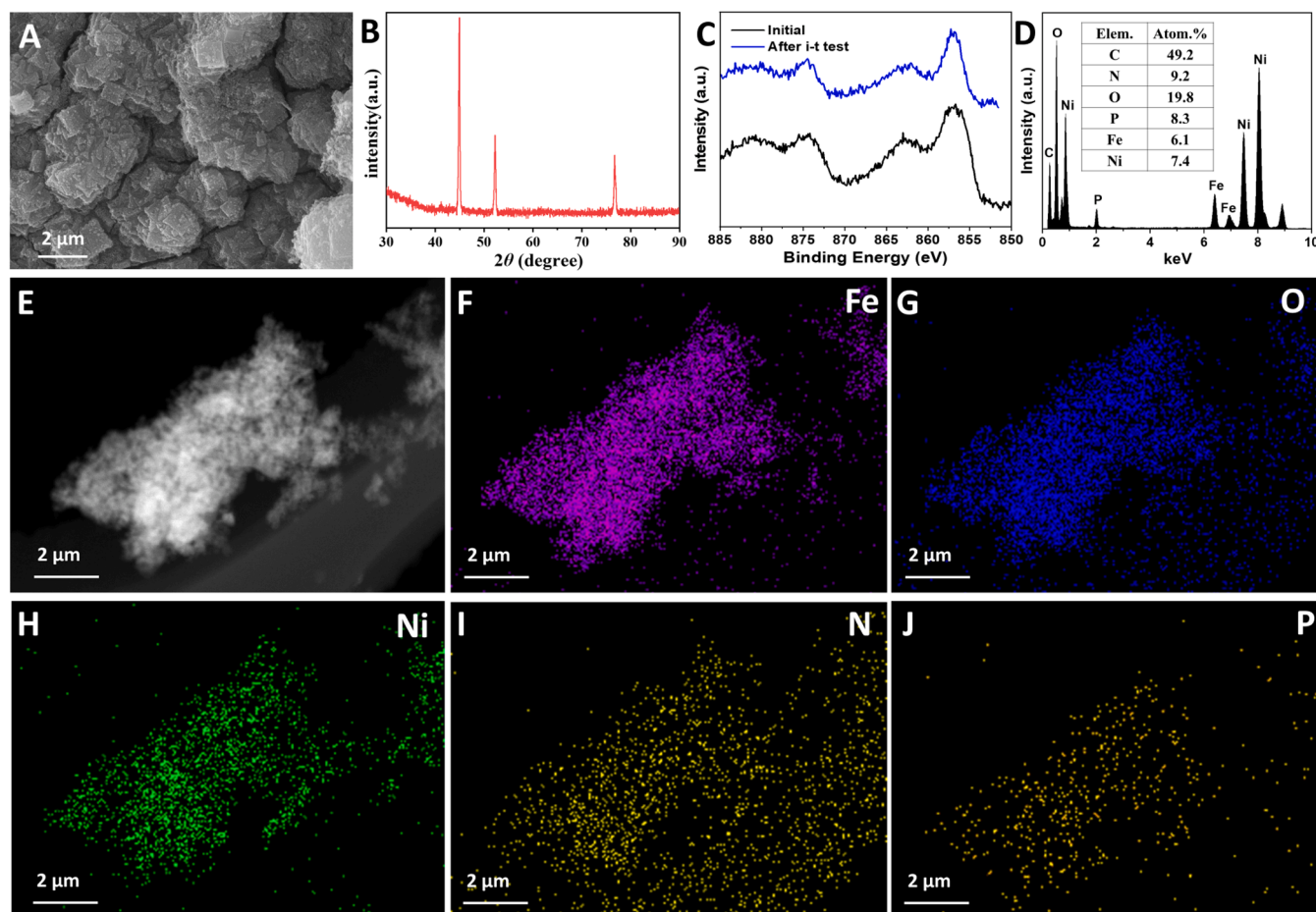


Fig. 7. Structural characterization of $\text{FeNi-C}_3\text{N}_4\text{-P}$ catalyst after chronoamperometric test. (A) SEM image, (B) XRD pattern, (C) High-resolution XPS spectra of Ni, (D) EDS spectra and composition, (E) HADDF-STEM image and the corresponding elemental mapping of (F) Fe, (G) O, (H) Ni, (I) N and (J) P.

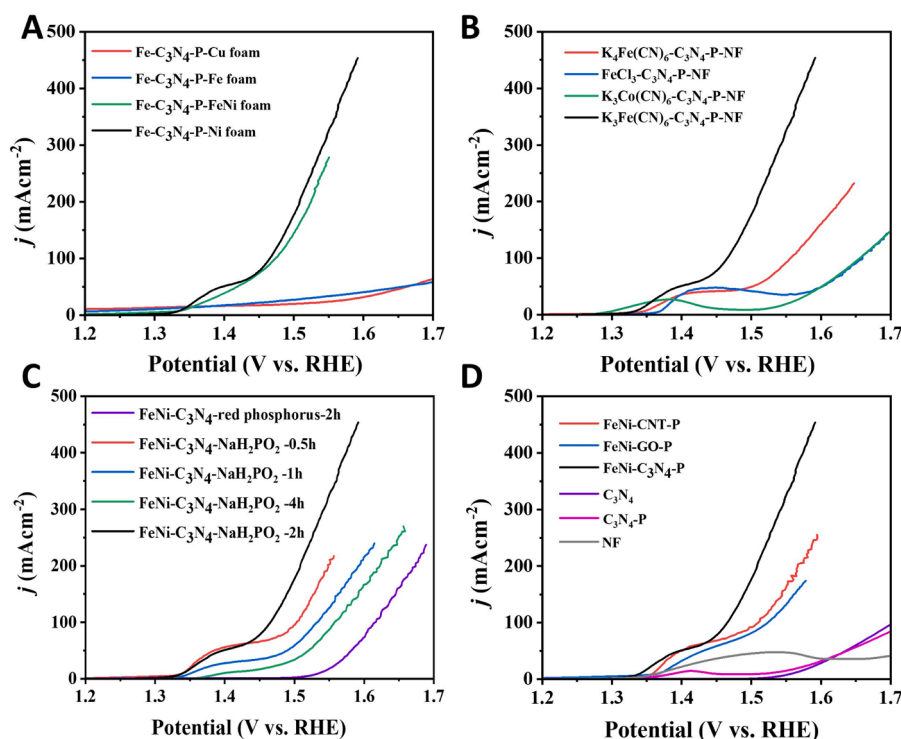


Fig. 8. The influence of composition and synthesis conditions. (A) The difference among Cu foam, Fe foam, Ni foam and NiFe foam, (B) The difference when using $K_3Fe(CN)_6$, $K_4Fe(CN)_6$, $K_3Co(CN)_6$ and $FeCl_3$. (C) The performances with different phosphating time and red phosphorus. (D) The performances with different carbon sources, carbon nano tube (CNT), graphene oxide (C) and C_3N_4 .

(CN)₆ cannot etch the Ni foam surface, resulting in too few Ni ions entering the catalyst layer to form sufficient Ni_2P . Therefore, the use of $K_3Fe(CN)_6$ as a precursor is crucial as it has the dual purpose of oxidizing the Ni foam surface and providing Fe source to form the desired FeNi-MOF structure [45]. Fig. 8 C compared the influence of phosphating time and phosphorus source. The catalyst with a phosphating time of 2 h showed better performance than those with phosphating times of 0.5 h, 1.0 h and 4 h. In addition, Fig. 8C also shows that the performance of the catalyst synthesized with NaH_2PO_2 as phosphorus source is better than that of red phosphorus. Fig. 8D compared the effect of different carbon substrates on the catalytic performance. C_3N_4 is a better substrate than carbon nanotubes (CNT) and graphene oxide (GO), possibly due to the presence of nitrogen (N). In addition, C_3N_4 and P-doped C_3N_4 (C_3N_4 -P) loaded on Ni foam display little catalytic activity below 1.55 V. Although Ni phosphide may also form in P-doped C_3N_4 , the amount of Ni phosphide produced is insufficient to catalyze the OER. From the experiments described above, it can be concluded that the use of $K_3Fe(CN)_6$, C_3N_4 , NaH_2PO_2 , and nickel foam is critical for the superior performance of the FeNi- C_3N_4 -P catalyst. The physically mixed FeNi-P catalyst exhibits a slightly lower onset OER potential compared to FeNi- C_3N_4 , indicating the superior catalytic activity of metal phosphide over FeNi-PBA (Fig. S14). However, at higher overpotentials, the OER current density of FeNi-P is lower than that of FeNi- C_3N_4 , potentially due to increased interfacial resistance and a blocked porous structure. These factors can also account for the observed lower performance of mixed FeNi-P compared to FeNi-P. Additionally, the presence of phase separation between FeP and NiP in mixed FeNi-P weakens the modulation effect between the Fe and Ni components, further contributing to the differences in catalytic performance.

4. Conclusion

In summary, modulating the NiFe-P catalyst with interfacial C_3N_4 can simultaneously improve the Ni sites and active the Fe sites. This

modulation optimizes the electronic configurations of Ni and Fe sites, as well as the adsorption configuration and the adsorption strength of oxygen-containing intermediates. As a result, the NiFe- C_3N_4 -P catalyst exhibited exceptional OER catalytic performance, including a small Tafel slope of 40.4 mV dec^{-1} , a low overpotential of 235 mV at a current density of 100 mA cm^{-2} , and excellent stability over a 58-h chronoamperometric test. These findings provide valuable insights and suggest an effective strategy for engineering highly active interfacial OER electrocatalysts.

CRediT authorship contribution statement

Hongyan Zhang: Formal analysis: Lead; Investigation: Lead. **Tao Yang:** Formal analysis: Lead; Investigation: Lead; Methodology: Lead; Project administration: Lead; Resources: Lead; Supervision: Lead. **Hao Zhou:** Data curation: Lead; Formal analysis: Equal; Investigation: Supporting. **Yikai Wang:** Data curation: Supporting; Investigation: Supporting. **Xuehan Yang:** Data curation: Supporting; Investigation: Supporting. **Wenjie Liang:** Investigation: Supporting. **Dan Wu:** Investigation: Supporting. **Pan Yuan:** Investigation: Supporting. **Tingting Yu:** Formal analysis: Supporting; Investigation: Supporting. **Maoshuai He:** Data curation: Supporting; Investigation: Supporting. **Wenxian Wei:** Data curation: Supporting; Investigation: Supporting.

Declaration of Competing Interest

The authors declare that they have no known competing financial interests or personal relationships that could have appeared to influence the work reported in this paper.

Data availability

Data will be made available on request.

Acknowledgements

This work was financially supported by the Natural Science Foundation of Jiangsu Province (No. BK20201466), the "521" Project of Lianyungang (LYG06521202132), the Key University Science Research Project of Jiangsu Province (No. 19KJA430007), and the project funded by the Priority Academic Program Development of Jiangsu Higher Education Institutions (PAPD).

Appendix A. Supporting information

Supplementary data associated with this article can be found in the online version at doi:10.1016/j.apcatb.2023.123391.

References

- [1] H.A. Gasteiger, N.M. Marković, Just a dream—or future reality? *Science* 324 (2009) 48–49.
- [2] S. Mallapaty, How China could be carbon neutral by mid-century, *Nature* 586 (2020) 482–483.
- [3] D.R. Gamelin, Water splitting: catalyst or spectator? *Nat. Chem.* 4 (2012) 965–967.
- [4] Z.-Y. Yu, Y. Duan, X.-Y. Feng, X. Yu, M.-R. Gao, S.-H. Yu, Clean and affordable hydrogen fuel from alkaline water splitting: past, recent progress, and future prospects, *Adv. Mater.* 33 (2021), 2007100.
- [5] N.-T. Suen, S.-F. Hung, Q. Quan, N. Zhang, Y.-J. Xu, H.M. Chen, Electrocatalysis for the oxygen evolution reaction: recent development and future perspectives, *Chem. Soc. Rev.* 46 (2017) 337–365.
- [6] N. Govindarajan, G. Kastlunger, H.H. Heenen, K. Chan, Improving the intrinsic activity of electrocatalysts for sustainable energy conversion: where are we and where can we go? *Chem. Sci.* 13 (2022) 14–26.
- [7] M. Chatenet, B.G. Pollet, D.R. Dekel, F. Dionigi, J. Deseure, P. Millet, R.D. Braatz, M.Z. Bazant, M. Eikerling, I. Staffell, P. Balcombe, Y. Shao-Horn, H. Schäfer, Water electrolysis: from textbook knowledge to the latest scientific strategies and industrial developments, *Chem. Soc. Rev.* 51 (2022) 4583–4762.
- [8] Q. Shi, C. Zhu, D. Du, Y. Lin, Robust noble metal-based electrocatalysts for oxygen evolution reaction, *Chem. Soc. Rev.* 48 (2019) 3181–3192.
- [9] Z.-P. Wu, X.F. Lu, S.-Q. Zang, X.W. Lou, Non-noble-metal-based electrocatalysts toward the oxygen evolution reaction, *Adv. Funct. Mater.* 30 (2020), 1910274.
- [10] Y. Shi, B. Zhang, Recent advances in transition metal phosphide nanomaterials: synthesis and applications in hydrogen evolution reaction, *Chem. Soc. Rev.* 45 (2016) 1529–1541.
- [11] C.-C. Weng, J.-T. Ren, Z.-Y. Yuan, Transition metal phosphide-based materials for efficient electrochemical hydrogen evolution: a critical review, *ChemSusChem* 13 (2020) 3357–3375.
- [12] A. Ray, S. Sultana, L. Paramanik, K.M. Parida, Recent advances in phase, size, and morphology-oriented nanostructured nickel phosphide for overall water splitting, *J. Mater. Chem. A* 8 (2020) 19196–19245.
- [13] P.F. Liu, X. Li, S. Yang, M.Y. Zu, P. Liu, B. Zhang, L.R. Zheng, H. Zhao, H.G. Yang, Ni₂P(O)/Fe₂P(O) interface can boost oxygen evolution electrocatalysis, *ACS Energy Lett.* 2 (2017) 2257–2263.
- [14] X. Wang, H. Zhong, S. Xi, W.S.V. Lee, J. Xue, Understanding of oxygen redox in the oxygen evolution reaction, *Adv. Mater.* 34 (2022), 2107956.
- [15] W. Guo, T. Yang, H. Zhang, H. Zhou, W. Wei, W. Liang, Y. Zhou, T. Yu, H. Zhao, Charge-counterbalance modulated amorphous nickel oxide for efficient alkaline hydrogen and oxygen evolution, *Chem. Eng. J.* 470 (2023), 144241.
- [16] L. Wu, L. Yu, F. Zhang, B. McElhenny, D. Luo, A. Karim, S. Chen, Z. Ren, Heterogeneous bimetallic phosphide Ni₂P-Fe₂P as an efficient bifunctional catalyst for water/seawater splitting, *Adv. Funct. Mater.* 31 (2021), 2006484.
- [17] Y. Li, H. Zhang, M. Jiang, Q. Zhang, P. He, X. Sun, 3D self-supported Fe-doped Ni₂P nanosheet arrays as bifunctional catalysts for overall water splitting, *Adv. Funct. Mater.* 27 (2017), 1702513.
- [18] F. Yu, H. Zhou, Y. Huang, J. Sun, F. Qin, J. Bao, W.A. Goddard, S. Chen, Z. Ren, High-performance bifunctional porous non-noble metal phosphide catalyst for overall water splitting, *Nat. Commun.* 9 (2018) 2551.
- [19] C.-F. Li, L.-J. Xie, J.-W. Zhao, L.-F. Gu, H.-B. Tang, L. Zheng, G.-R. Li, Interfacial Fe–O–Ni–O–Fe Bonding Regulates the Active Ni Sites of Ni-MOFs via Iron Doping and Decorating with FeOOH for Super-Efficient Oxygen Evolution, *Angew. Chem. Int. Ed.* 61 (2022), e202116934.
- [20] G. Zhang, J. Zeng, J. Yin, C. Zuo, P. Wen, H. Chen, Y. Qiu, Iron-facilitated surface reconstruction to in-situ generate nickel-iron oxyhydroxide on self-supported FeNi alloy fiber paper for efficient oxygen evolution reaction, *Appl. Catal. B Environ.* 286 (2021), 119902.
- [21] C.-J. Huang, H.-M. Xu, T.-Y. Shuai, Q.-N. Zhan, Z.-J. Zhang, G.-R. Li, A review of modulation strategies for improving catalytic performance of transition metal phosphides for oxygen evolution reaction, *Appl. Catal. B Environ.* 325 (2023), 122313.
- [22] F. Pan, T. Jin, W. Yang, H. Li, Y. Cao, J. Hu, X. Zhou, H. Liu, X. Duan, Theory-guided design of atomic Fe–Ni dual sites in N,P-co-doped C for boosting oxygen evolution reaction, *Chem. Catal.* 1 (2021) 734–745.
- [23] B. Zhang, X. Zheng, O. Voznyy, R. Comin, M. Bajdich, M. García-Melchor, L. Han, J. Xu, M. Liu, L. Zheng, F.P. García de Arquer, C.T. Dinh, F. Fan, M. Yuan, E. Yassitepe, N. Chen, T. Regier, P. Liu, Y. Li, P. De Luna, A. Janmohamed, H.L. Xin, H. Yang, A. Vojvodic, E.H. Sargent, Homogeneously dispersed multimetal oxygen-evolving catalysts, *Science* 352 (2016) 333–337.
- [24] M. Jiang, H. Zhai, L. Chen, L. Mei, P. Tan, K. Yang, J. Pan, Unraveling the Synergistic Mechanism of Bi-Functional Nickel–Iron Phosphides Catalysts for Overall Water Splitting, *Adv. Funct. Mater.*, n/a 2302621.
- [25] S. Lee, L. Bai, X. Hu, Deciphering iron-dependent activity in oxygen evolution catalyzed by nickel–iron layered double hydroxide, *Angew. Chem. Int. Ed.* 59 (2020) 8072–8077.
- [26] W. Li, Y. Chen, B. Yu, Y. Hu, X. Wang, D. Yang, 3D hollow Co–Fe–P nanoframes immobilized on N,P-doped CNT as an efficient electrocatalyst for overall water splitting, *Nanoscale* 11 (2019) 17031–17040.
- [27] T. Li, G. Luo, Q. Liu, S. Li, Y. Zhang, L. Xu, Y. Tang, J. Yang, H. Pang, Encapsulation of NiCo nanoparticles into foam-like porous N,P-codoped carbon nanosheets: electronic and architectural dual regulations toward high-efficiency water electrolysis, *Chem. Eng. J.* 410 (2021), 128325.
- [28] W. Li, B. Yu, Y. Hu, X. Wang, B. Wang, X. Zhang, D. Yang, Z. Wang, Y. Chen, Encapsulating hollow (Co,Fe)P nanoframes into N,P-codoped graphene aerogel for highly efficient water splitting, *J. Power Sources* 456 (2020), 228015.
- [29] Y.-N. Wang, Z.-J. Yang, D.-H. Yang, L. Zhao, X.-R. Shi, G. Yang, B.-H. Han, FeCoP₂ nanoparticles embedded in N and P co-doped hierarchically porous carbon for efficient electrocatalytic water splitting, *ACS Appl. Mater. Interfaces* 13 (2021) 8832–8843.
- [30] Y. Zheng, Y. Jiao, Y. Zhu, Q. Cai, A. Vasileff, L.H. Li, Y. Han, Y. Chen, S.-Z. Qiao, Molecule-level g-C₃N₄ coordinated transition metals as a new class of electrocatalysts for oxygen electrode reactions, *J. Am. Chem. Soc.* 139 (2017) 3336–3339.
- [31] X. Chen, R. Hu, DFT-based study of single transition metal atom doped g-C₃N₄ as alternative oxygen reduction reaction catalysts, *Int. J. Hydrog. Energy* 44 (2019) 15409–15416.
- [32] J. Zheng, T. Kang, B. Liu, P. Wang, H. Li, M. Yang, N-doped carbon nanotubes encapsulated with FeNi nanoparticles derived from defect-rich, molecule-doped 3D g-C₃N₄ as an efficient bifunctional electrocatalyst for rechargeable zinc–air batteries, *J. Mater. Chem. A* 10 (2022) 9911–9921.
- [33] G. Kresse, J. Furthmüller, Efficient iterative schemes for ab initio total-energy calculations using a plane-wave basis set, *Phys. Rev. B* 54 (1996) 11169–11186.
- [34] G. Kresse, D. Joubert, From ultrasoft pseudopotentials to the projector augmented-wave method, *Phys. Rev. B* 59 (1999) 1758–1775.
- [35] J.P. Perdew, K. Burke, M. Ernzerhof, Generalized gradient approximation made simple, *Phys. Rev. Lett.* 77 (1996) 3865–3868.
- [36] I.L. Novak, F. Gao, P. Kraikivski, B.M. Slepchenko, Diffusion amid random overlapping obstacles: similarities, invariants, approximations, *J. Chem. Phys.* 134 (2011).
- [37] L. Bai, C.-S. Hsu, D.T.L. Alexander, H.M. Chen, X. Hu, A cobalt–iron double-atom catalyst for the oxygen evolution reaction, *J. Am. Chem. Soc.* 141 (2019) 14190–14199.
- [38] Z. Zhu, K. Xu, W. Guo, H. Zhang, X. Xiao, M. He, T. Yu, H. Zhao, D. Zhang, T. Yang, Vanadium-phosphorus incorporation induced interfacial modification on cobalt catalyst and its super electrocatalysis for water splitting in alkaline media, *Appl. Catal. B Environ.* 304 (2022), 120985.
- [39] W. Guo, T. Yang, H. Zhang, H. Zhou, M. He, W. Wei, W. Liang, Y. Zhou, T. Yu, H. Zhao, Fe and Mo co-modulated coral-like nickel pyrophosphate in-situ derived from nickel-foam for oxygen evolution, *ChemSusChem*, n/a e202300633.
- [40] W. Wang, L. Du, R. Xia, R. Liang, T. Zhou, H.K. Lee, Z. Yan, H. Luo, C. Shang, D. L. Phillips, Z. Guo, In situ protonated-phosphorus interstitial doping induces long-lived shallow charge trapping in porous C₃–xN₄ photocatalysts for highly efficient H₂ generation, *Energy Environ. Sci.* 16 (2023) 460–472.
- [41] Y.-P. Zhu, T.-Z. Ren, Z.-Y. Yuan, Mesoporous phosphorus-doped g-C₃N₄ nanostructured flowers with superior photocatalytic hydrogen evolution performance, *ACS Appl. Mater. Interfaces* 7 (2015) 16850–16856.
- [42] X. Wang, B. Wang, Y. Chen, M. Wang, Q. Wu, K. Srinivas, B. Yu, X. Zhang, F. Ma, W. Zhang, Fe₂P nanoparticles embedded on Ni₂P nanosheets as highly efficient and stable bifunctional electrocatalysts for water splitting, *J. Mater. Sci. Technol.* 105 (2022) 266–273.
- [43] L. Yan, Y. Sun, E. Hu, J. Ning, Y. Zhong, Z. Zhang, Y. Hu, Facile in-situ growth of Ni₂P/Fe₂P nanohybrids on Ni foam for highly efficient urea electrolysis, *J. Colloid Interface Sci.* 541 (2019) 279–286.
- [44] L. Yin, X. Ding, W. Wei, Y. Wang, Z. Zhu, K. Xu, Z. Zhao, H. Zhao, T. Yu, T. Yang, Improving catalysis for electrochemical water splitting using a phosphosulphide surface, *Inorg. Chem. Front.* 7 (2020) 2388–2395.
- [45] D.I. Jeong, H.W. Choi, J. Kim, U.Y. Lee, B.K. Koo, B.K. Kang, D.H. Yoon, Ni₂P/Fe₂P encapsulated in N, P co-doped carbon shell as overall water splitting catalyst for wide pH range electrochemical applications, *Appl. Surf. Sci.* 614 (2023), 156189.
- [46] H. Qiu, Q. Ma, X. Sun, X. Han, G. Jia, Y. Zhang, W. He, Facile synthesis of g-C₃N₄/LDH self-growing nanosheet arrays for enhanced supercapacitor performance, *J. Alloy. Compd.* 896 (2022), 163023.
- [47] Z. Yu, Y. Li, J. Qu, R. Zheng, J.M. Cairney, J. Zhang, M. Zhu, A. Khan, W. Li, Enhanced photoelectrochemical water-splitting performance with a hierarchical heterostructure: Co₃O₄ nanodots anchored TiO₂@P-C₃N₄ core-shell nanorod arrays, *Chem. Eng. J.* 404 (2021), 126458.
- [48] J. Yang, D. Guo, S. Zhao, Y. Lin, R. Yang, D. Xu, N. Shi, X. Zhang, L. Lu, Y.-Q. Lan, J. Bao, M. Han, Cobalt phosphides nanocrystals encapsulated by P-doped carbon and married with p-doped graphene for overall water splitting, *Small* 15 (2019), 1804546.

- [49] J. Chang, Y. Xiao, M. Xiao, J. Ge, C. Liu, W. Xing, Surface oxidized cobalt-phosphide nanorods as an advanced oxygen evolution catalyst in alkaline solution, *ACS Catal.* 5 (2015) 6874–6878.
- [50] R. Zhang, Z. Wei, G. Ye, G. Chen, J. Miao, X. Zhou, X. Zhu, X. Cao, X. Sun, “d-electron complementation” induced V-Co phosphide for efficient overall water splitting, *Adv. Energy Mater.* 11 (2021), 2101758.
- [51] P. He, X.-Y. Yu, X.W. Lou, Carbon-incorporated nickel–cobalt mixed metal phosphide nanoboxes with enhanced electrocatalytic activity for oxygen evolution, *Angew. Chem. Int. Ed.* 56 (2017) 3897–3900.
- [52] H. Zhang, W. Zhou, J. Dong, X.F. Lu, X.W. Lou, Intramolecular electronic coupling in porous iron cobalt (oxy)phosphide nanoboxes enhances the electrocatalytic activity for oxygen evolution, *Energy Environ. Sci.* 12 (2019) 3348–3355.
- [53] Q. Wang, R. He, F. Yang, X. Tian, H. Sui, L. Feng, An overview of heteroatom doped cobalt phosphide for efficient electrochemical water splitting, *Chem. Eng. J.* 456 (2023), 141056.
- [54] X. Hu, R. Wang, W. Feng, C. Xu, Z. Wei, Electrocatalytic oxygen evolution activities of metal chalcogenides and phosphides: fundamentals, origins, and future strategies, *J. Energy Chem.* 81 (2023) 167–191.
- [55] M.B. Stevens, L.J. Enman, A.S. Batchellor, M.R. Cosby, A.E. Vise, C.D.M. Trang, S. W. Boettcher, Measurement techniques for the study of thin film heterogeneous water oxidation electrocatalysts, *Chem. Mater.* 29 (2017) 120–140.
- [56] C.-C. Hou, H.-F. Wang, C. Li, Q. Xu, From metal–organic frameworks to single/dual-atom and cluster metal catalysts for energy applications, *Energy Environ. Sci.* 13 (2020) 1658–1693.
- [57] Y. Xu, R. Wang, J. Wang, Y. Zhang, T. Jiao, Encapsulation of Fe-CoP with P, N-codoped porous carbon matrix as a multifunctional catalyst for wide electrochemical applications, *J. Energy Chem.* 71 (2022) 36–44.
- [58] Y. Dou, C.-T. He, L. Zhang, H. Yin, M. Al-Mamun, J. Ma, H. Zhao, Approaching the activity limit of CoSe₂ for oxygen evolution via Fe doping and Co vacancy, *Nat. Commun.* 11 (2020) 1664.
- [59] J. Lin, P. Wang, H. Wang, C. Li, X. Si, J. Qi, J. Cao, Z. Zhong, W. Fei, J. Feng, Defect-rich heterogeneous MoS₂/NiS₂ nanosheets electrocatalysts for efficient overall water splitting, *Adv. Sci.* 6 (2019), 1900246.
- [60] D. Wang, Q. Li, C. Han, Q. Lu, Z. Xing, X. Yang, Atomic and electronic modulation of self-supported nickel–vanadium layered double hydroxide to accelerate water splitting kinetics, *Nat. Commun.* 10 (2019) 3899.
- [61] L. Huang, G. Gao, H. Zhang, J. Chen, Y. Fang, S. Dong, Self-dissociation-assembly of ultrathin metal–organic framework nanosheet arrays for efficient oxygen evolution, *Nano Energy* 68 (2020), 104296.
- [62] P. Li, X. Duan, Y. Kuang, Y. Li, G. Zhang, W. Liu, X. Sun, Tuning electronic structure of nife layered double hydroxides with vanadium doping toward high efficient electrocatalytic water oxidation, *Adv. Energy Mater.* 8 (2018), 1703341.
- [63] W. Li, X. Gao, D. Xiong, F. Xia, J. Liu, W.-G. Song, J. Xu, S.M. Thalluri, M. F. Cerqueira, X. Fu, L. Liu, Vapor–solid synthesis of monolithic single-crystalline CoP nanowire electrodes for efficient and robust water electrolysis, *Chem. Sci.* 8 (2017) 2952–2958.
- [64] N. Jiang, B. You, M. Sheng, Y. Sun, Electrodeposited cobalt-phosphorous-derived films as competent bifunctional catalysts for overall water splitting, *Angew. Chem. Int. Ed.* 54 (2015) 6251–6254.
- [65] B. You, N. Jiang, M. Sheng, S. Gul, J. Yano, Y. Sun, High-performance overall water splitting electrocatalysts derived from cobalt-based metal–organic frameworks, *Chem. Mater.* 27 (2015) 7636–7642.
- [66] W. Li, X. Gao, X. Wang, D. Xiong, P.-P. Huang, W.-G. Song, X. Bao, L. Liu, From water reduction to oxidation: Janus Co-Ni-P nanowires as high-efficiency and ultrastable electrocatalysts for over 3000h water splitting, *J. Power Sources* 330 (2016) 156–166.
- [67] L. Yu, L. Wu, B. McElhenny, S. Song, D. Luo, F. Zhang, Y. Yu, S. Chen, Z. Ren, Ultrafast room-temperature synthesis of porous S-doped Ni/Fe (oxy)hydroxide electrodes for oxygen evolution catalysis in seawater splitting, *Energy Environ. Sci.* 13 (2020) 3439–3446.
- [68] L. Yu, Q. Zhu, S. Song, B. McElhenny, D. Wang, C. Wu, Z. Qin, J. Bao, Y. Yu, S. Chen, Z. Ren, Non-noble metal-nitride based electrocatalysts for high-performance alkaline seawater electrolysis, *Nat. Commun.* 10 (2019) 5106.
- [69] L. Wu, L. Yu, Q. Zhu, B. McElhenny, F. Zhang, C. Wu, X. Xing, J. Bao, S. Chen, Z. Ren, Boron-modified cobalt iron layered double hydroxides for high efficiency seawater oxidation, *Nano Energy* 83 (2021), 105838.
- [70] X. Zhang, H. Zhao, C. Li, S. Li, K. Liu, L. Wang, Facile coordination driven synthesis of metal–organic gels toward efficiently electrocatalytic overall water splitting, *Appl. Catal. B Environ.* 299 (2021), 120641.
- [71] Y.-J. Tang, L. You, K. Zhou, Enhanced oxygen evolution reaction activity of a Co₂P@NC–Fe₂P composite boosted by interfaces between a N-Doped carbon matrix and Fe₂P microspheres, *ACS Appl. Mater. Interfaces* 12 (2020) 25884–25894.
- [72] D. Li, C. Zhou, R. Yang, Y. Xing, S. Xu, D. Jiang, D. Tian, W. Shi, Interfacial engineering of the CoxP–Fe₂P heterostructure for efficient and robust electrochemical overall water splitting, *ACS Sustain. Chem. Eng.* 9 (2021) 7737–7748.
- [73] S. Wang, P. Yang, X. Sun, H. Xing, J. Hu, P. Chen, Z. Cui, W. Zhu, Z. Ma, Synthesis of 3D heterostructure Co-doped Fe₂P electrocatalyst for overall seawater electrolysis, *Appl. Catal. B Environ.* 297 (2021), 120386.
- [74] C. Huang, Y. Zou, Y.-Q. Ye, T. Ouyang, K. Xiao, Z.-Q. Liu, Unveiling the active sites of Ni–Fe phosphide/metaphosphate for efficient oxygen evolution under alkaline conditions, *Chem. Commun.* 55 (2019) 7687–7690.
- [75] J. Xu, J. Li, D. Xiong, B. Zhang, Y. Liu, K.-H. Wu, I. Amorim, W. Li, L. Liu, Trends in activity for the oxygen evolution reaction on transition metal (M = Fe, Co, Ni) phosphide pre-catalysts, *Chem. Sci.* 9 (2018) 3470–3476.